ORIGINAL ARTICLE

**Francisco Bodziony · Xiaomei Li · Mariana Yin ·
Rüdiger Berger · Hans-Jürgen Butt · Holger Marschall**

Contribution of wedge and bulk viscous forces in droplets moving on inclined surfaces

Abstract Employing direct numerical simulations, we investigate water and water-glycerol (85 wt%) droplets (~25 μL) moving on smooth surfaces, with contact angles of around 90°, at varying inclinations. Our focus is on elucidating the relative contribution of local viscous forces in the wedge and bulk regions in droplets to the total viscous force. We observe that, for fast-moving droplets, both regions contribute comparably, while the contribution of the wedge region dominates in slow-moving cases. Comparisons with existing estimates reveal the inadequacy of previous predictions in capturing the contributions of wedge and bulk viscous forces in fast-moving droplets. Furthermore, we demonstrate that droplets with identical velocities can exhibit disparate viscous forces due to variations in internal fluid dynamics.

1 Introduction

Liquid drops wetting surfaces are common both in the natural and industrial world. The prediction of such drop motions has far-reaching implications in many fields of application, including phase change heat transfer [1,2], microfluidics[3], flow control [4], coating technology [5], and the biomedical field [6,7].

The motion of a single droplet on an inclined surface has been extensively studied by experimental, numerical and theoretical methods [8–10]. These studies focus primarily on the droplet shape and steady-state velocity, the contact angle hysteresis and also the critical inclination angle. Still the behavior of droplets on

F. Bodziony (✉) · H. Marschall (✉)
Computational Multiphase Flow Group, Department of Mathematics, Technical University Darmstadt, Peter-Grünberg-Straße 10, 64287 Darmstadt, Hessen, Germany
E-mail: francisco.bodziony@tu-darmstadt.de

H. Marschall
E-mail: holger.marschall@tu-darmstadt.de

X. Li · R. Berger · H.-J. Butt
Max Planck Institute for Polymer Research, Ackermannweg 10, 55128 Mainz, Rhineland-Palatinate, Germany
E-mail: lix2@mpip-mainz.mpg.de

R. Berger
E-mail: berger@mpip-mainz.mpg.de

H.-J. Butt
E-mail: butt@mpip-mainz.mpg.de

M. Yin
Department of Chemical Engineering, Instituto Superior Técnico, Av. Rovisco Pais 1, 1049-001 Lisbon, Portugal
E-mail: mariana.ye.yin@tecnico.ulisboa.pt
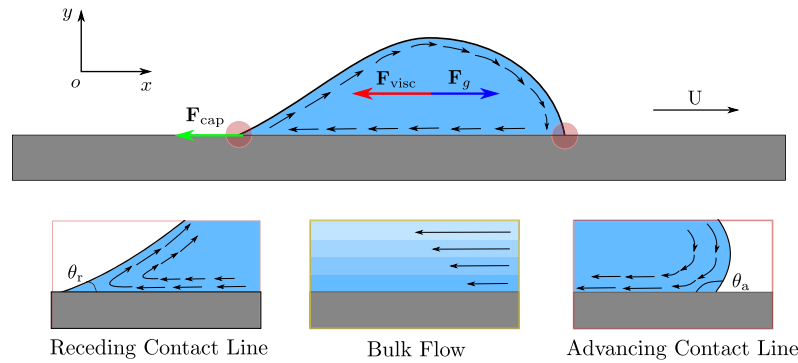
Fig. 1 Forces acting on a sliding droplet

an inclined solid surface remains poorly understood. Of particular interest is the contribution of local viscous forces that oppose droplet motion, which require further elucidation and quantification.

For a grounded substrate, the motion of a droplet is governed by the balance between the gravitational force, driving the motion of the droplet, and the viscous forces in the bulk and wedge regions and contact line friction forces which counteract, as illustrated in Fig. 1.

Historically, the examination of forces acting on droplets has predominantly relied on experimental analysis of droplet motion induced by gravity on tilted substrates [11–13]. Other experimental setups have also been employed, where force-calibrated cantilevers [14–16] and oscillating droplet tribometer [17] setups have been used to quantify the friction force of moving droplets. However, accurately quantifying the viscous forces acting on droplets during motion remains a nontrivial task. A comprehensive overview of various approaches as well as current challenges is given in [18].

To bridge this knowledge gap, we employ Computational Fluid Dynamics (CFD) as a tool to investigate the interactions among gas, liquid, and solid phases during the motion of droplets on inclined planar substrates. Through direct numerical simulations (DNS), where all relevant spatio-temporal scales are resolved, it is possible to accurately simulate the motion of a droplet and comprehensively quantify the underlying processes. CFD provides additional valuable insights and understanding of critical aspects of droplet motion that are not easily accessible through experimental means. Specifically, we focus on identifying and characterizing the viscous forces acting on a droplet moving down an inclined plane.. Another question that we address is how these viscous forces are influenced by the droplet velocity, and the relative contribution of local viscous forces in the wedge and bulk regions of these droplets.

Previous studies have employed numerical simulations to investigate the spreading and motion of droplets [1,19,20]. These simulations have primarily focused on the development of numerical methods capable of accurately capturing these processes, involving investigations of critical contact angles, droplet shape, and steady-state velocities, which are then compared to experimental and numerical results [21–23]. While these numerical simulations have led to significant insights on the processes associated with droplet motion, there remains a noticeable gap in the literature concerning a systematic assessment of the forces acting on the droplet during motion, particularly the contribution of viscous forces.

In this study, we use a phase-field approach to simulate the motion of droplets moving on a tilted planar substrate, for both water and a water-glycerol (85 wt%) mixture. The utilization of a diffuse interface model is crucial as it enables the representation of a moving three-phase contact line in conjunction with the no-slip condition at the solid–liquid interface, allowing for accurate depiction of transient wetting processes with contact line dynamics [24]. This approach is thermodynamically grounded in an energy variational formulation that governs the evolution of the phase by minimizing the free energy of the system [25]. As a result, the interface is approached physically rather than numerically. It is fundamentally distinct from the Volume-Of-Fluid (VOF) and Level-Set methods, which are based on sharp interface modeling. Previous work by Jamshidi et al. [26] has highlighted the limitations of the standard VOF methods in predicting accurate physics, while the Phase-Field (PF) method achieved high accuracy when the diffuse interface was suitably resolved. Our simulations utilize the diffuse-interface phase-field solver `phaseFieldFoam`, implemented in OpenFOAM (FOAM-extend 5.0), which has undergone extensive validation for various cases of static and dynamic wetting on both simple and complex substrates, including chemically patterned surfaces [27].

2 Numerical method

Assuming immiscible Newtonian fluids under isothermal and isochoric conditions, the Navier–Stokes equations within the diffuse interface phase-field methodology are

$$\nabla \cdot \mathbf{u} = 0, \tag{1a}$$

$$\partial_t(\rho \mathbf{u}) + \nabla \cdot (\rho \mathbf{u} \otimes \mathbf{u}) = -\nabla \tilde{p} + \nabla \cdot [\mu(\nabla \mathbf{u} + \nabla \mathbf{u}^\mathsf{T})] + \rho \mathbf{g} - \nabla \cdot (\mathbf{u} \otimes \mathbf{J}) + \mathbf{f}_s. \tag{1b}$$

Herein, $\otimes$ denotes the dyadic product, $\mathbf{u}$ is the flow velocity and $\mathbf{g}$ is the gravity vector. The diffusive phase-field mass flux is given as $\mathbf{J} = \frac{1}{2}\sum_{p=1}^{N}\rho \mathbf{J}_p$, and $\rho = \sum_{p=1}^{N}\rho_p\frac{C_p+1}{2}$ and $\mu = \sum_{p=1}^{N}\mu_p\frac{C_p+1}{2}$ represent the average density and dynamic viscosity, where C_p is the phase-field order parameter for phase p.

Note that we use a modified pressure $\tilde{p} = p + \frac{f_m}{2}$, since the gradient term $\nabla\frac{f_m}{2}$ can be extracted from the Korteweg stress term, which accounts for capillarity, and can be absorbed into the pressure gradient term [28], i.e., $\frac{1}{2}\sum_{p,q=1}^{N}\nabla \cdot (\lambda_{p,q}\nabla C_p \otimes \nabla C_q) = \frac{1}{2}\sum_{p=1}^{N}\Phi_p\nabla C_p + \nabla\frac{f_m}{2}$. Hence, $\mathbf{f}_s = \frac{1}{2}\sum_{p=1}^{N}\Phi_p\nabla C_p$. The term $\nabla \cdot (\mathbf{u} \otimes \mathbf{J})$ is required for thermodynamic consistency, for a system of non-matched densities [29].

The evolution of the order parameters C_p for a system of N immiscible phases is given by the Cahn-Hilliard equation, as

$$\partial_t C_p + \nabla \cdot (C_p \mathbf{u}) = -\nabla \cdot \mathbf{J}_p, \quad 1 \leqslant p \leqslant N. \tag{2}$$

where the phase-field flux is

$$\boldsymbol{J}_p = \sum_{q=1}^{N} -M_{p,q}\nabla \Phi_q, \quad 1 \leqslant p \leqslant N, \tag{3}$$

Here, Φ_q is the chemical potential of phase q and $M_{p,q}$ is the mobility between phases p and q,

$$M_{p,q} = \begin{cases} -M_0(1+C_p)(1+C_q), & p \neq q \\ M_0(1+C_p)(1-C_q), & p = q \end{cases}, \quad 1 \leqslant q, p \geqslant N, \tag{4}$$

where M_0 is a non-negative mobility constant.

In the spirit of Cahn and Hilliard, the chemical potential is obtained from the variational derivative of the mixing free energy of the system (also called the Helmholtz free energy), viz.

$$\Phi_p = \frac{\delta F_m}{\delta C_p}, \tag{5}$$

where the total free energy F is given as the sum of the mixing energy, F_m and the wall free energy density, F_w, viz.

$$F = F_m + F_w = \int_\Omega f_m \, \mathrm{d}\mathbf{x} + \int_{\partial\Omega} f_w \, \mathrm{d}s. \tag{6}$$

Here, Ω denotes the fluid domain and $\partial\Omega$ represents its boundary, a solid surface not permeable to fluids. f_m and f_w denote the local mixing energy density and the local wall energy density, respectively. For a two-phase system, the mixing energy density can be expressed [30] as

$$f_m(C_p, \nabla C_p) = \lambda_{p,q}\left(\frac{1}{2}|\nabla C_p|^2 + \frac{1}{\varepsilon^2}\Psi(C_p)\right). \tag{7}$$

The first term on the right-hand side of (7) represents the gradient energy, which characterizes the interfacial energy density and accounts for non-local interactions promoting complete mixing of the fluids. The second term, known as the bulk energy density, models the tendency of the components to separate [31].

Here, $\lambda_{p,q}$ is the mixing energy between phase p and q, ε is the capillary width and $\Psi(C_p)$ denotes a double-well potential, which is usually taken as the Ginzburg-Landau potential,

$$\Psi(C_p) = \frac{1}{4}(C_p^2 - 1)^2. \tag{8}$$

With Eqs. (5), (7) and (8) we can compute the chemical potential of phase p as

$$\Phi_p = \lambda_{p,q} \left(\frac{1}{\varepsilon^2} \Psi'_p(C_p) + \nabla^2 C_p \right). \tag{9}$$

From this, the equilibrium interfacial profile can be obtained. Requiring $\Phi_p = 0$ and a planar interface yields

$$C_p(n) = \tanh\left(\frac{n}{\sqrt{2}\epsilon} \right), \tag{10}$$

where n is the interface normal vector field. Within $3/\sqrt{2}\varepsilon$, it can be shown that the order parameter C_p varies from about -0.9 to 0.9. Note that the tangent hyperbolic profile in Eq. (10) is only valid for the Ginzburg-Landau potential, and changing the double-well potential used would change the interfacial profile.

Assuming such a planar diffuse interface in equilibrium, the mixing energy coefficient $\lambda_{p,q}$ is related to the surface tension coefficient employed in sharp interface models by [31,32]

$$\lambda_{p,q} = \frac{3}{2\sqrt{2}} \sigma \varepsilon. \tag{11}$$

Wetting boundary condition

For a diffuse interface in contact with a wall, the wall free energy density has to be considered. It can be written for a system of two fluids as

$$f_w(C_p) = \sigma_{SL} + (\sigma_{SG} - \sigma_{SL})\Psi_w(C_p), \tag{12}$$

where $\Psi_w(C_p)$ satisfies the bulk limits $\Psi_w(-1) = 0$ and $\Psi_w(1) = 1$. Equation (12) postulates that the wall free energy density is a function only of the fluid composition next to the wall [31]. By performing a variational procedure and integrating by parts, we obtain

$$\lambda_{p,q} \partial_n C_p + f'_w(C_p) = 0, \tag{13}$$

where $f'_w(C_p) = (\sigma_{SG} - \sigma_{SL})\Psi'_w(C_p)$ denotes the derivative of the wall free energy density with respect to the order parameter C_p. Equation (13) is commonly referred to as the wetting condition, as it describes the diffusive relaxation process of the dynamic contact angle toward the equilibrium angle to leading order [24,31,32].

For the chosen $\Psi(C_p)$, it can be shown that

$$f_w(C_p) = \sigma \cos\theta_0 \frac{C_p\left(C_p^2 - 3\right)}{4} + \frac{\sigma_{wp} + \sigma_{wq}}{2}. \tag{14}$$

Herein, the interfacial tension coefficients between the wall and fluid p (with $C_p = 1$) are denoted by σ_{wp}, and between wall and fluid q (with $C_p = -1$) by σ_{wq}, respectively [24].

Using Eqs. (13) and (14), we arrive at the wetting boundary condition,

$$\partial_n C_p = \frac{\cos\theta_0}{\sqrt{2}\epsilon} \left(1 - C_p^2 \right), \tag{15}$$

which determines the interface shape close to the wall.

Since zero flux across the wall is required,

$$\partial_n \Phi_p = 0. \tag{16}$$

Despite the classic no-slip boundary condition being applied, the contact line moves. This is owed to the higher order diffusion term in (2).

Table 1 Physical properties

Fluid	Density (kg/m^3)	Kinematic Viscosity (m^2/s)
Water	1000	1.00E-06
Glycerol (85 wt%)	1222	9.25E-05
Air	1	1.00E-05
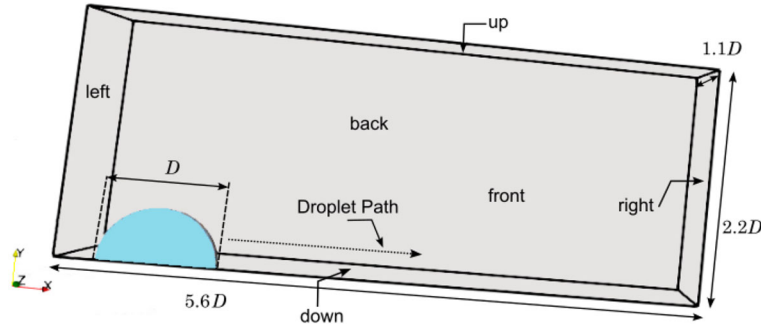
Fig. 2 Computational domain with parametrized dimensions

3 Validation

Our `phaseFieldFoam` solver has undergone rigorous validation to establish its accuracy in simulating static and dynamic (de-)wetting phenomena [27,33–36]. This validation process involved a comparison of the solver's predictions with experimental data [37,38], confirming its ability to effectively capture intricate interfacial dynamics. The numerical stability, convergence, and consistency of the solver across various scenarios have also been evaluated using theoretical benchmarks [26,39].

4 Computational setup

4.1 Physical properties

A droplet in the form of a spherical cap is initially placed on an inclined plane. The physical properties of the employed liquids, water and water-glycerol (85 wt%), as well as of the surrounding air are given in Table 1. Densities and kinematic viscosities are chosen to match the real physical situation for a constant temperature of $25\,^oC$. The droplet has a volume of 25 µL, the initial diameter is 4.5 mm and it is subjected to gravitational force. The surface tension of water with air and water-glycerol (85 wt%) with air are 0.072 N/m and 0.064 N/m, respectively.

Based on the contact angle hysteresis [40], a static contact angle of $\theta_0 = 82°$ and $\theta_0 = 103°$ have been calculated for the water/air and water-glycerol/air (85 wt%) systems, respectively. The contact angle hysteresis for water is $(\theta_a, \theta_r) = (95°, 78°)$ and for water-glycerol it is $(\theta_a, \theta_r) = (111°, 100°)$, which are taken from experimental measurements. Due to the nature of the model being based on the wall chemical potential, see Equation (15), the contact angles varying with contact line velocities are inherently captured according to Cox-Voinov—see [25] for details.

4.2 Case description

All the simulations are three-dimensional with a computational domain of $0.025 \times 0.010 \times 0.005$ m. Figure 2 shows a schematic illustration of the computational domain with parameterized dimensions. Table 2 provides the boundary conditions.

The computational cost of solving the Navier–Stokes Cahn-Hilliard equations is closely tied to the number of control volumes used, meaning that reducing the control volume count results in shorter simulation times and lower computational costs. By utilizing the symmetryPlane boundary condition, which takes advantage of

Table 2 Boundary conditions

	c_p, c_q	**u**	$\tilde{p}$	Φ_p, Φ_q
Right	zeroGradient	zeroGradient	fixedValue	zeroGradient
Down	equilibriumPhaseContactAngle	fixedValue	fixedFluxPressure	zeroGradient
Left	zeroGradient	zeroGradient	fixedValue	zeroGradient
Up	zeroGradient	fixedValue	zeroGradient	zeroGradient
Back	zeroGradient	zeroGradient	zeroGradient	zeroGradient
Front	symmetryPlane	symmetryPlane	symmetryPlane	symmetryPlane

the droplet's symmetry, the computational domain is effectively halved, further optimizing the computational efficiency. On the bottom wall, the wetted substrate, Eq. (15) is applied as a boundary condition for the phase-field equation. As the bottom wall is impermeable, a no-penetration condition applies and $\mathbf{n}_w \cdot \mathbf{J_p} = \mathbf{n}_w \cdot (-M\nabla\Phi_p) = 0$. Since the mobility is a constant, this results into a zero-gradient condition for the chemical potential Φ_p. A fixed zero pressure and zero-gradient for the velocity are combined to provide an open boundary at the top, the back, and the side of the domain. A no-slip condition is applied for the velocity at the wall patch.

The mobility parameter is set to scale with $\sim M \times \epsilon^2$. The time-step is adjusted based on the maximum Courant number $\mathrm{Co_{max}}$, which is limited to 0.02, and the maximum time-step is initially specified as 5×10^{-6} s, in this work.

For all simulations, a sufficiently small Cahn number of $\mathrm{C_n} = \varepsilon/W = 0.01$, where W denotes the characteristic length (in this case, the droplet's initial radius), has been applied, which ensures that the correct physics of the interface is captured.

4.3 Adaptive mesh refinement

To achieve precise simulation outcomes while mitigating excessive computational expenses, an adaptive mesh refinement (AMR) technique is employed. In this approach, a fine mesh is selectively generated for regions surrounding the interface and inside the droplet, whereas a relatively coarse grid is utilized for the less critical air phase. Consequently, both the total number of cells within the computational domain and the overall computation time are significantly reduced.

The mesh cells are of hexahedral shape in this study. Their minimum size is approximately 45 μm, which sets the lower limit for the resolved length scales pertaining to the internal flow dynamics of the droplet.

4.4 Calculation of relevant forces

In the remainder, we attempt to analyze and discuss viscous forces inside the moving droplets. In particular, the contributions from the wedge and bulk regions of droplets are investigated. Note that the viscous stress tensor in the momentum Eq. (1b) is

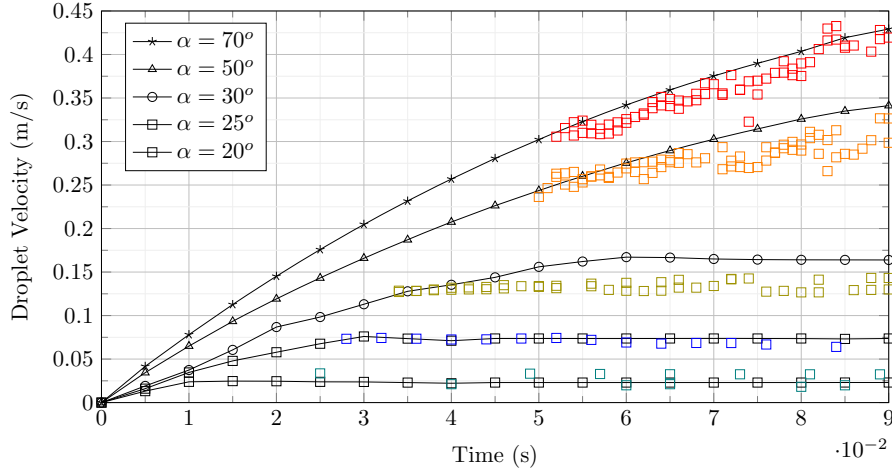$$\boldsymbol{\tau} = \mu(\nabla\mathbf{u} + \nabla\mathbf{u}^\mathsf{T}). \tag{17}$$

Taking the divergence of the stress tensor, the volumetric viscous force density is computed as

$$\mathbf{f}_{\mathrm{visc}}^{\mathrm{total}} = \nabla \cdot \boldsymbol{\tau}. \tag{18}$$

The viscous stress term if then expanded:

$$\begin{aligned}
\nabla \cdot \boldsymbol{\tau} &= \nabla \cdot \left(\mu(\nabla\mathbf{u} + \nabla\mathbf{u}^\mathsf{T})\right) \\
&= \nabla \cdot (\mu\nabla\boldsymbol{u}) + \nabla \cdot \left(\mu\nabla\mathbf{u}^\mathsf{T}\right) \\
&= \nabla \cdot (\mu\nabla\boldsymbol{u}) + (\nabla\boldsymbol{u}) \cdot \nabla\mu + \mu\nabla(\nabla \cdot \boldsymbol{u}) \\
&= \nabla \cdot (\mu\nabla\boldsymbol{u}) + (\nabla\boldsymbol{u}) \cdot \nabla\mu,
\end{aligned} \tag{19}$$

which allows for a semi-implicit discretization of the viscous stress term.

Fig. 3 Water drop velocity over time for various inclination angles α. The scatter points represent the experimental data, and the lines with markers the simulation data

Integrating Eq. (18) over the droplet volume Ω_L, we get the total viscous force in Eq. (20):

$$\mathbf{F}_{\text{visc}}^{\text{total}} = \int_{\Omega_L} \mathbf{f}_{\text{visc}}^{\text{total}} \, \mathrm{d}V. \tag{20}$$

The term "total" refers to the fact that the integration has been performed over the entire droplet volume, i.e., we have not distinguished at this point bulk from wedge contributions. However, this is of particular interest and thus will be subject to discussion based on post-processing of the local data being set out hereafter.

The viscous stress exerted to the wall can then be computed using (17) as

$$\boldsymbol{\tau}_w = \boldsymbol{\tau} \cdot \boldsymbol{n}_w - \boldsymbol{n}_w (\boldsymbol{n}_w \cdot \boldsymbol{\tau}), \tag{21}$$

where $\boldsymbol{n}_w$ is the outer unit normal of the boundary wall. With this, the total viscous force exerted onto the wetted wall is

$$\mathbf{F}_{\text{visc}}^{\text{wall}} = \int_{\Omega_L} \boldsymbol{\tau}_{\boldsymbol{w}} \, \mathrm{d}S. \tag{22}$$

5 Results and discussion

5.1 Droplet velocities

For validation, we have compared the droplets' barycenter velocity and the droplet shape from experiments to our simulation results. Details about the experimental setup and data can be taken from [41]. The velocities of water droplets have been varied by changing the inclination angle $\alpha \in \{20°, 25°, 30°, 50°, 70°\}$. The results are shown in Fig. 3. Moreover, we have compared our simulation results with the velocity of water droplets measured in experiments. Experimentally, the drop is placed onto the tilted plane. In doing so, the droplet assumes already an initial velocity when the measurement starts. For the numerical simulations, however, the droplet has been initialized as a semi-sphere with no initial velocity. Because of these different initial conditions, it is only possible to compare the droplet velocities at later times, particularly at higher inclination angles, i.e., larger droplet velocities. The results are shown in Fig. 3. We observe a very good agreement for all simulated droplets with experimental measurements. This agreement with experimental results is upheld over a wide range of substrate inclination angles.

Moreover, the droplet velocities and shapes at quasi-steady-state have been evaluated and compared to experimental data. The results in Figs. 4 and 5 show again a very good agreement with the experiments. Note that we have only compared velocities of droplets on substrates with an inclination angle of up to 30°. The
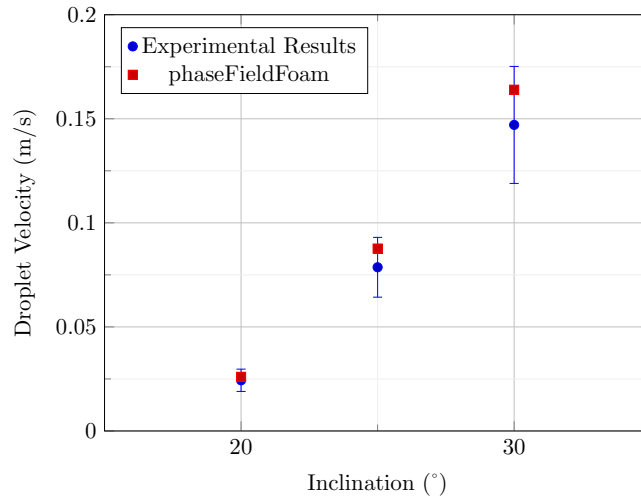
Fig. 4 Comparison of water droplet velocities at quasi-steady-state at inclinations of 20°, 25° and 30°
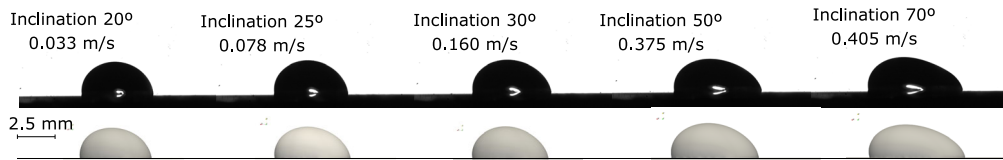
Fig. 5 Shapes of a water droplet ($\sim 25\,\mu$L) during their motion on tilted plates of various inclination angles. Bottom row: Numerical simulation results, top row: experimental images

reason is that, at higher inclinations, the size of the tilted plate used in the experiments has been found to be not long enough for the droplets to reach their terminal velocities.

Figure 6 shows the obtained velocities of glycerol-water (85 wt%) droplets for plate inclination angles of 15°, 30° and 40°. Not that, for all inclinations and different as for the water droplets, the droplet velocities peak (at $t \sim 0.01$ s) and then fall to stabilize to the respective droplet terminal velocities. Maglio & Legendre (2014) observe the same for their study of wetting of high-viscosity fluids [22]. Here, we don't compare the transient velocities of water-glycerol droplets with the ones from experiments, as by the time the droplet velocity is measured experimentally, it has long reached quasi-steady-state velocity. Note that for the largest inclination there is still a small increase of the droplet velocity. Apart from this, the droplet acceleration here is approximately zero, i.e., the values obtained at 0.07 s are very close to the terminal velocities. This is further substantiated in Fig. 7 which shows that the droplet terminal velocities obtained in experiments and from simulations are in very good agreement. Figure 8 depicts the shapes of the water-glycerol droplets from the simulations and from the experimental measurements. Again, a very good agreement is observed. Summarizing, we conclude that our simulation results are of physical fidelity and we can proceed with their analysis.

5.2 Viscous forces

5.2.1 Viscous force density

Figure 9 depicts the simulation results for a water droplet moving on a substrate with 70° tilt at various instances of different velocities, showing the local the viscous forces inside the moving droplets.

We observe that the viscous force is higher in the wetted area (and especially in near the contact line) due to the large local shear between the liquid and the solid. Note that the smallest length scale we resolve corresponds to the size of the computational cells adjacent to the wall which have a height of 45 μm.

Based on experimental studies performed by Dussan and Davis [42], De Gennes [43] attributed this to the rolling motion of the flow near the edges of the droplet, giving rise to regions of high viscous friction. Moffatt
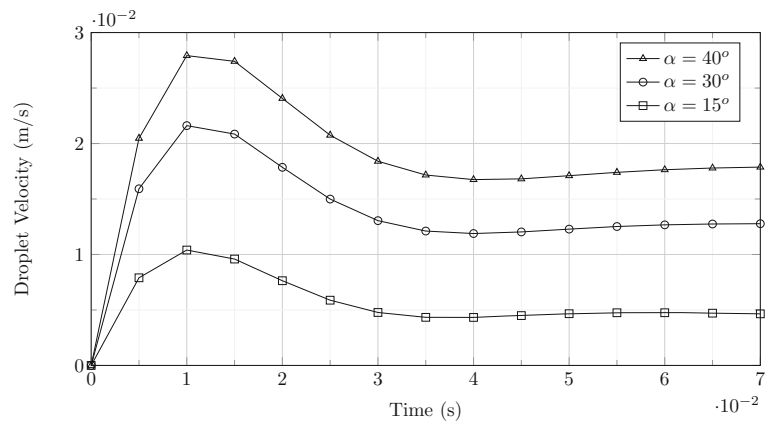
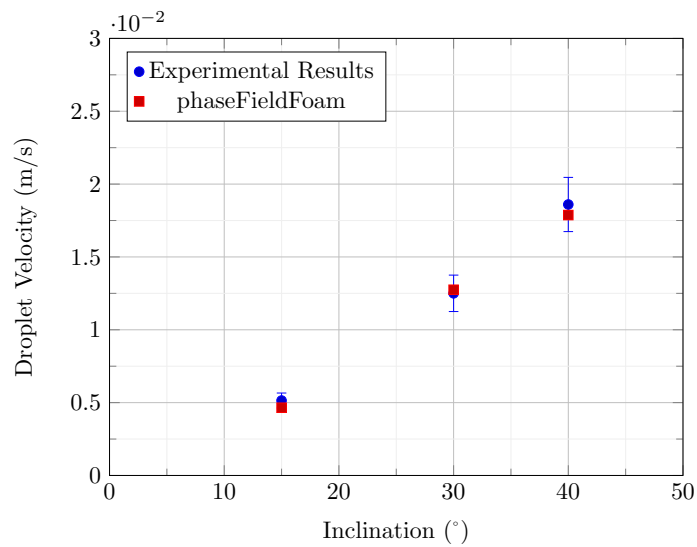**Fig. 6** Water-glycerol (85 wt%) drop velocity over time for various inclination angles

Fig. 7 Comparison of water-glycerol (85 wt%) droplet velocities at quasi-steady-state at inclinations of 15°, 30° and 45°
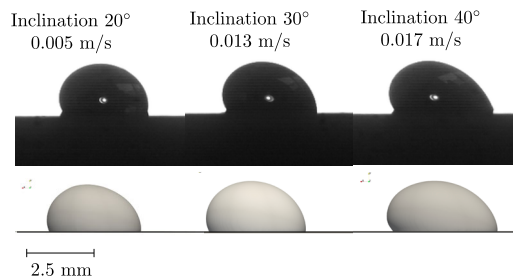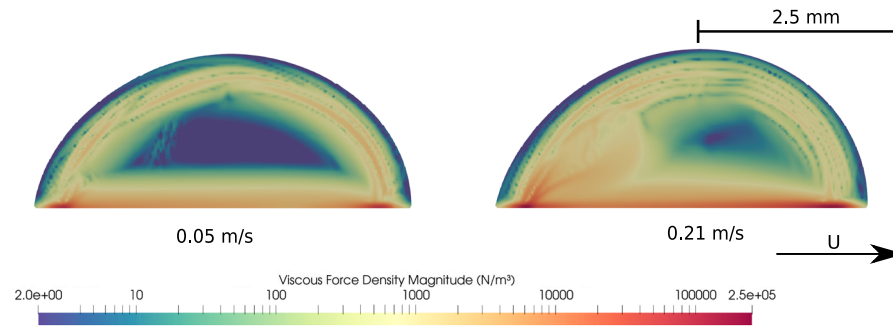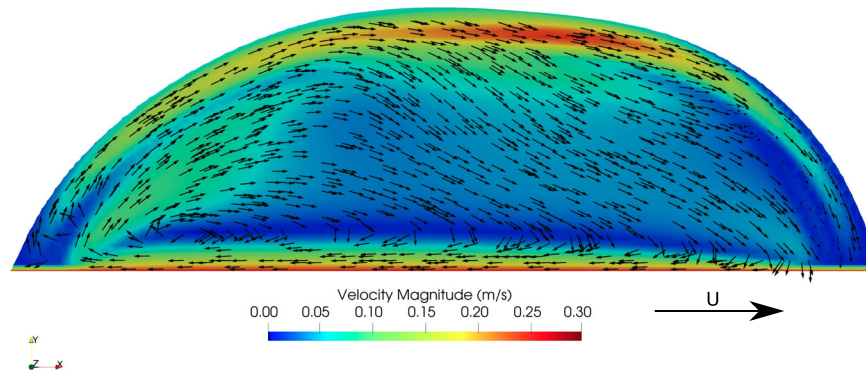

Fig. 8 Shapes of a water-glycerol droplet ($\sim 25\,\mu L$) during their motion on tilted plates of various inclination angles. Bottom row: numerical simulation results, top row: experimental images

Fig. 9 Side view on the cutting plane through the center of a water droplet moving on a substrate showing the viscous force density magnitude at different velocities

Fig. 10 Simulation result of velocity field and internal flow, for a water droplet moving at 0.28 m/s. The velocity vectors shown here are computed in a co-moving reference frame

[44] has credited these high shear rates to the formation of eddies near the corner of a plane and a free surface, although such a solution is only valid for asymptotically small Reynolds numbers.

Away from the contact line, within the wetted substrate region, the viscous force is orders of magnitude lower. We observe, for higher droplet velocities, that the friction substantially increases. There is an increase in the local viscous force close to the interface region. The liquid near the substrate moves in the opposite direction to the droplet motion. Continuity, however, requires the liquid in the bulk of the droplet to move in the direction of droplet motion. This flow counter to the flow near the substrate establishes somewhere within the bulk close to the interface (Fig. 10), giving rise to higher velocity gradients there and thus higher viscous forces.

Note that we do not discuss the contribution of contact line friction, as this channel of dissipation is negligible for the length and time scales that we are concerned with [45].

Underlying the typical free-surface assumption (no parallel shear stress at the interface), we compute the area-specific viscous force density $\mathbf{f}_{visc}^{wall}$ only at the wall instead the volumetric viscous force density. This then allows the discrimination between the contributions of viscous force densities in bulk and wedge regions, to which we will call bulk and wedge viscous forces, respectively. To verify the free surface assumption, Fig. 11 depicts the comparison of the total viscous force integrated over the droplet volume according to (20) with the boundary viscous force integrated over the contact area according to (22). One observes that the magnitude of the surface-averaged viscous force is slightly larger than that of the volume-averaged one. Particularly at high droplet velocities, this could be attributed to the deterioration of the interfacial equilibrium profile according to (10). Given that the deviation is small, we leave a detailed analysis for the future.

In Figs. 12 and 13 we show the viscous force density per unit area exerted to the substrate by a water and a water-glycerol droplet, respectively. Looking onto the area wetted by the droplet, the viscous force field is non-homogeneous, and the viscous force is highest in the vicinity of the contact line, mainly at the rear and front edges of the droplet (i.e., the wedge region). It can also be seen that inside this wedge region the viscous
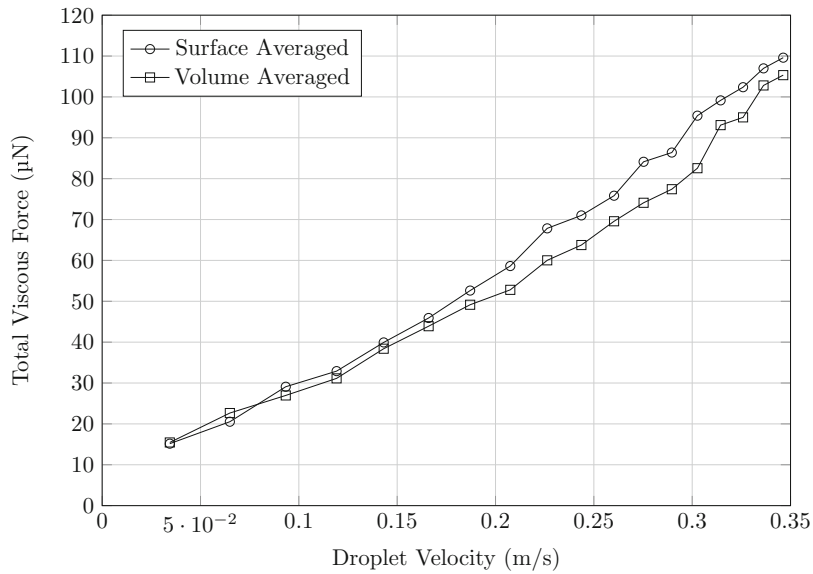
Fig. 11 Comparison between surface and the volume-averaged viscous force magnitudes

force is not uniformly distributed, and the front and rear edges contribute more to the wedge viscous force than the sides of the droplet.

One of the main difficulties in assessing the contribution of the wedge viscous force to the total viscous force is in quantifying the width of the wedge region. As the viscous force changes along the droplet perimeter, a pragmatic approach is needed to estimate the contribution of wedge viscous force to the overall viscous force. Therefore, we plot the values of $|\mathbf{f}_{\text{visc}}^{\text{wall}}|$ along lines AB and CD, as shown in Figs. 12 and 13 to estimate the wedge width. Here, we assume that the wedge region has a width equal to double the distance from the contact line to the peak in the magnitude of local viscous forces, which is depicted as gray-shaded area.

For water-glycerol droplets, the viscous force at the wedge is much larger than for water droplets, despite the higher velocities of water droplets. This is due to the viscosity of the glycerol-water mixture being almost 100 times larger than for pure water. Because the wedge viscous force scales inversely with the contact angle [13], the local viscous force density at the rear edge of the water-glycerol droplet is larger than at the front. Clearly, this can be attributed to the fact that the rear contact angle is lower than the advancing one, thus exhibiting a larger wedge viscous force. For water this is not the case, since the droplet is still accelerating, and the contact line velocity in the front edge is larger than at the rear edge.

The plots along the lines AB and CD in Figs. 12 and 13 reveal spatial variations in viscous force along the contact line, contrary to the expected maximum stress at this region. Surprisingly, the force peaks occur near the advancing and receding edges rather than directly at the contact line. Specifically, for water droplets, this peak is located approximately 200 to 400 μm away from the contact line, while for glycerol, it is around 100 μm away. This intriguing finding prompts the question of how the mesh resolution influences such force profiles and their temporal evolution. Therefore, the next section addresses the mesh sensitivity of our results.

5.2.2 Influence of mesh resolution

To investigate the influence of the applied mesh resolution on the accuracy of viscous forces predicted by our simulations, a mesh dependency study has been conducted. While previously we have shown that the applied mesh resolution is sufficient to accurately predict the quasi-steady-state velocity of water-glycerol droplets at various substrate inclinations, it does not guarantee that the viscous forces within the droplet, which is intricately linked to its internal flow, is accurately captured by the same mesh resolution.

In Fig. 14, the total viscous forces acting on an inclined substrate are plotted at different velocities of the water droplet, employing various mesh sizes. Meshes with 220k, 450k, and 700k cells were utilized, corresponding to cell sizes of approximately 80μm, 45μm, and 25μm, respectively. The inclination angle of 50° has been deliberately chosen for this mesh dependency study, as it is expected to exhibit significant velocity gradients during droplet motion. Accurate simulation capturing of these gradients is crucial to precisely
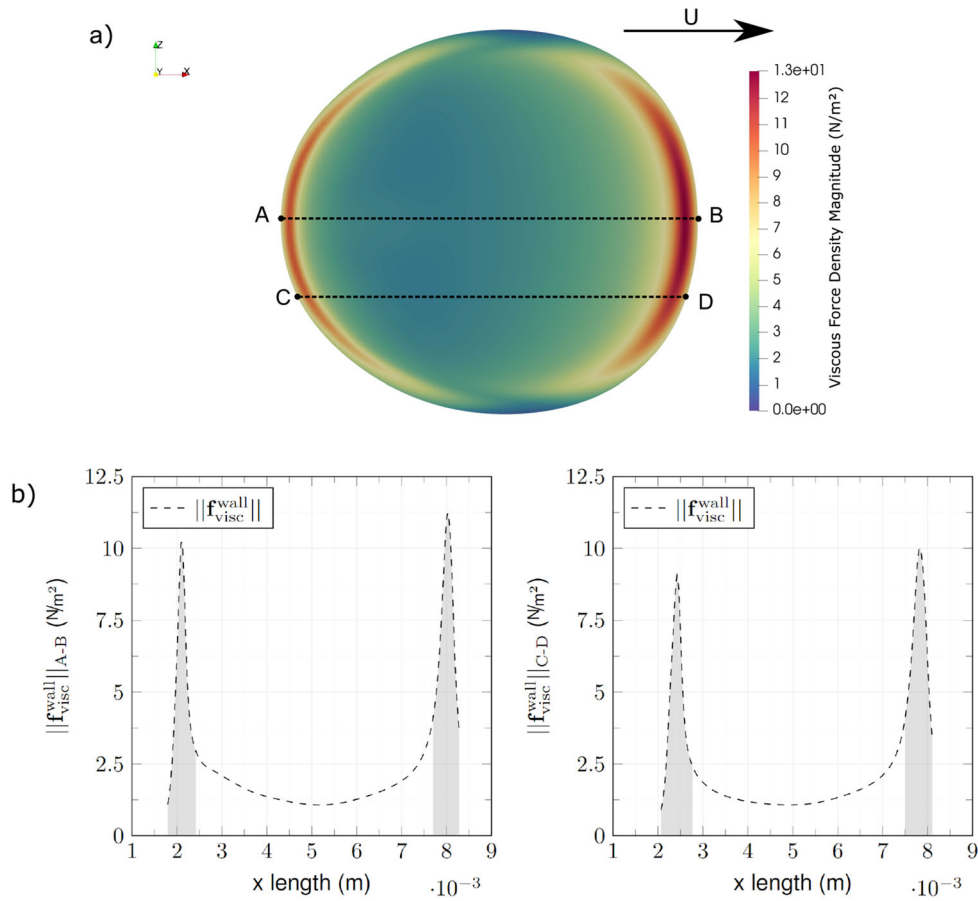
Fig. 12 Distribution of the magnitude of local viscous forces $\|\mathbf{f}_{\text{visc}}^{\text{wall}}\|$ on the wetted area of a water droplet, at substrate inclination angle of $\alpha = 50°$ and droplet velocity $U_p = 0.23$ m/s. The gray-shaded area represents the estimated wedge region

describe the contributions of both bulk and viscous forces. From the results depicted in Fig. 14, utilizing a mesh with approximately 450k cells, is a reasonable balance between capturing flow physics and minimizing computational cost, and thus this mesh resolution will be employed in this study.

5.2.3 Wedge and bulk viscous forces

In order to assess the contribution of wedge and bulk viscous forces during the sliding motion and how they change with sliding velocity, we calculate the ratio between the wedge viscous force and the total viscous force magnitudes.

Using an estimate of [46], the magnitude of the wedge viscous force is approximated to
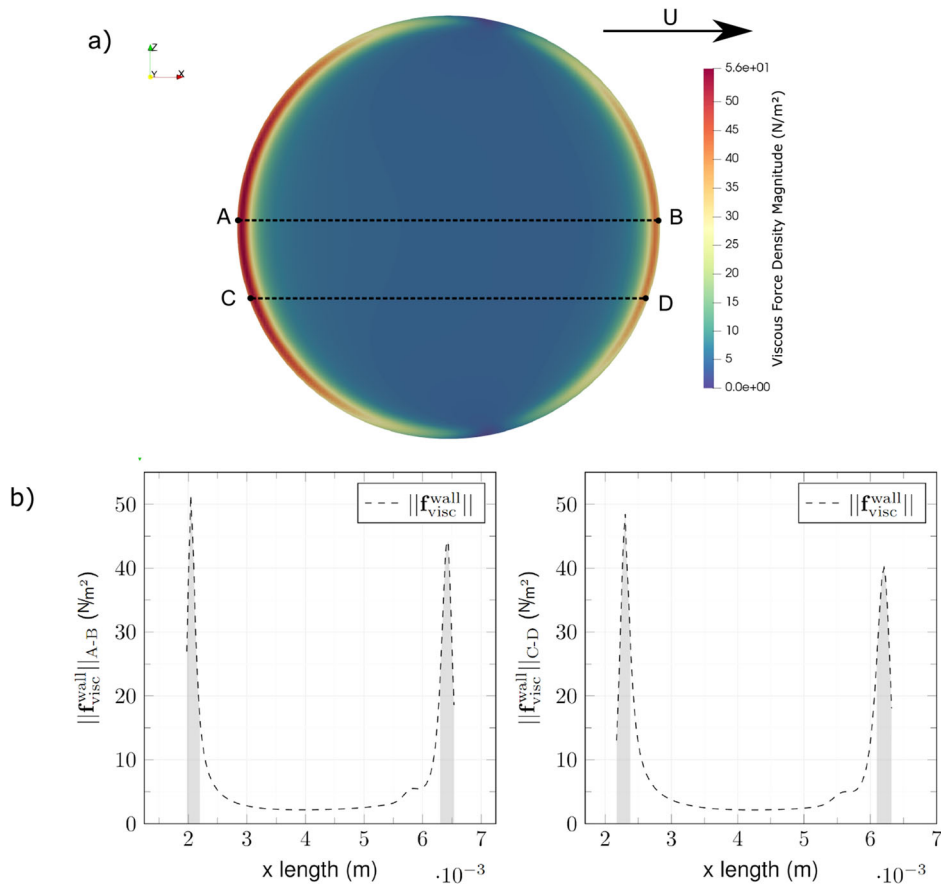
$$F_{\text{visc, est}}^{\text{wedge}} \approx 4w\mu U_P \ln \frac{L}{L_s}[c(\theta_a) + c(\theta_r)], \tag{23}$$

and the magnitude of the bulk viscous force as

$$F_{\text{visc, est}}^{\text{bulk}} \approx \frac{\mu \pi l w}{2h} U_P. \tag{24}$$

Herein, w denotes the droplet width, μ is the liquid viscosity, h is the droplet height, l its peripheral length, and $c(\theta)$ a function of the contact angle, given by

$$c(\theta) = \frac{\sin^2(\theta)}{2(\theta - \sin\theta\cos\theta)}. \tag{25}$$

Fig. 13 Distribution of the magnitude of local viscous forces $\|\mathbf{f}_{\mathrm{visc}}^{\mathrm{wall}}\|$ on the wetted area of a water-glycerol droplet, at substrate inclination angle $\alpha = 30°$ and droplet velocity $U_p = 0.011 \, \mathrm{m/s}$. The gray-shaded area represents the estimated wedge region
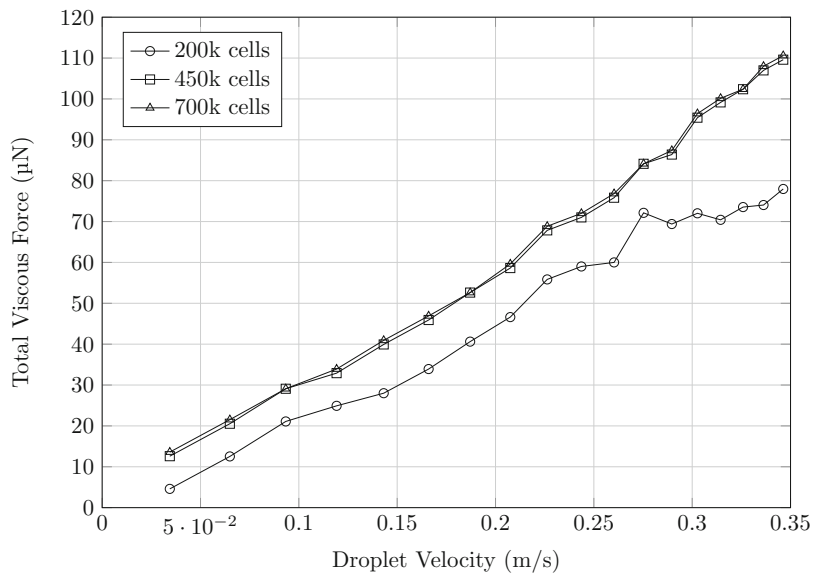
Fig. 14 Mesh dependency study performed for the simulation of a water droplet on an inclined substrate with 50° inclination, for meshes with approximately 220k, 450k and 700k cells
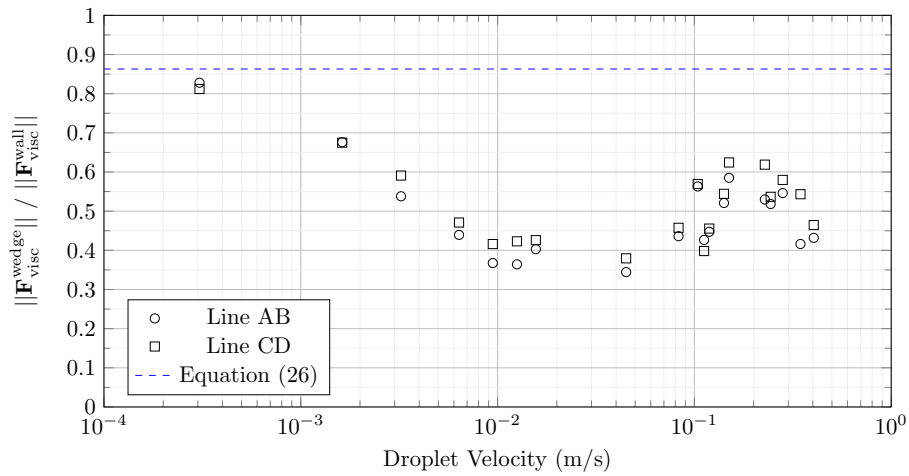
Fig. 15 Comparison of the relative contribution of the wedge to the total viscous force at various droplet velocities—Estimate according to Kim et al. [13] versus Results from local simulation data for a water droplet

Using (23) and (24), the estimated total viscous force then is $F_{\text{visc, est}}^{\text{total}} = F_{\text{visc, est}}^{\text{wedge}} + F_{\text{visc, est}}^{\text{bulk}}$. In Eq. (23), the wedge viscous force depends on both the advancing and receding contact angles. Furthermore, it contains the unknown term L/L_s. L is a macroscopic length, which is typically considered to be in the order of the droplet or the capillary length. L_s is the microscopic cut-off length, introduced to avoid divergence of the viscous shear stress at the contact line [47]. It describes the region where slip is allowed and extends typically over few molecular diameters [45,48]. We have used $L = 2.25\,\text{mm}$, which is the droplet initial radius, and $L_s = 1\,\text{nm}$, which is used commonly in literature.

Assuming that the droplet does not deform significantly, Kim et al. [13] have estimated the ratio between the wedge and the total viscous forces to be

$$\left(\frac{F_{\text{visc}}^{\text{wedge}}}{F_{\text{visc}}^{\text{total}}}\right)_{\text{est}} \approx \frac{1}{1 + \frac{1}{[c(\theta_a)+c(\theta_r)]ln(L/L_s)}}. \tag{26}$$

Using this approach, we estimate the relative contribution of wedge viscous force to the total viscous force and compare it with the simulation results for both water and glycerol droplet systems. Specifically, we analyze the local data along the lines AB and CD shown in Figs. 12 and 13 to investigate how the contribution of wedge viscous force varies along the droplet perimeter.

To quantify the ratio of contributions, we compare the shaded area, relating to the magnitude of the wedge viscous force $||\mathbf{F}_{\text{visc}}^{\text{wedge}}||$, with the total area under the curve, relating to the total viscous force $||\mathbf{F}_{\text{visc}}^{\text{wall}}||$. Figure 15 depicts the corresponding ratio for various water droplet velocities, revealing the extent of wedge contribution to the total viscous force. These results are then compared to the estimated ratio according to (26). To simplify the analysis, we assume that $[c(\theta_a) + c(\theta_r)]/2 \approx c(\theta_0)$, indicating that the mean value of the contact angle hysteresis is independent of the contact line velocity.

For low droplet velocities, the results align with the ratio determined by (26), indicating the dominance of wedge viscous force. During this initial stages of droplet motion, the friction originating from regions distant from the contact line is significantly lower compared to the friction occurring near the contact line. Consequently, the contribution of wedge viscous force is expected to be substantially higher than that of bulk viscous force, resulting in a high ratio of wedge viscous force in the low sliding velocity regime. However, at higher velocities, the contribution of wedge viscous force decreases to around 50%, deviating from the expected ratio.

In Fig. 16, we compare the wedge and bulk viscous forces computed from our simulation results with those obtained from estimates. By substituting experimentally measured values of droplet dimensions, advancing and receding contact angles, and droplet velocity into Eqs. (23) and (24), we estimate the wedge and bulk viscous forces ($F_{\text{visc, est}}^{\text{wedge}}$ and $F_{\text{visc, est}}^{\text{bulk}}$, respectively). Considering the experimental droplet velocities ranging from approximately $0.01\,\text{m/s}$ to $0.5\,\text{m/s}$, we assess the wedge and bulk viscous forces within this velocity range. From Fig. 15, we observe that the contribution of wedge viscous force remains relatively constant
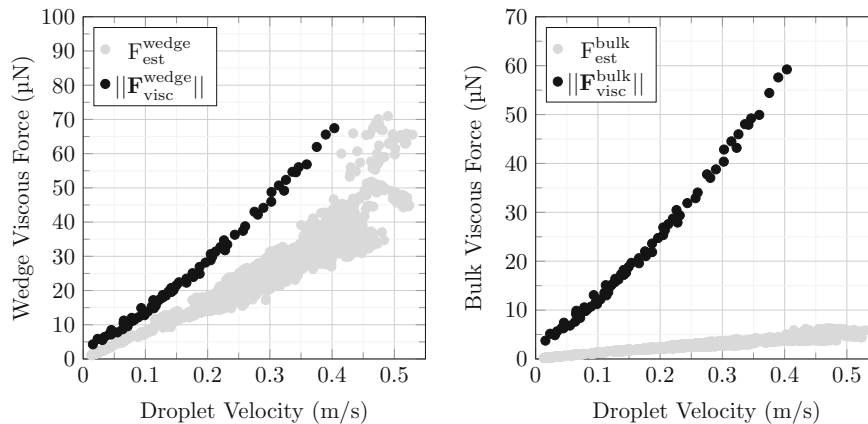
Fig. 16 Wedge (left) and bulk (right) viscous forces exerted by a water droplet, for the investigated range of droplet velocities

at around 53% of the total viscous force. This value is subsequently used to discriminate the wedge and bulk viscous forces, $||\mathbf{F}_{\text{visc}}^{\text{wedge}}||$ and $||\mathbf{F}_{\text{visc}}^{\text{bulk}}||$, from the total viscous force which has been calculated from the simulation results.

Clearly, Fig. 16 shows a significant discrepancy between simulation-based results and the experimental ones, where we have used (23) and (24). The estimation of the wedge viscous force involves fitting the unknown parameter L/L_s to the simulation results. However, this yields an unrealistic value of approximately 1×10^{17}. Such a value is physically implausible as it would require sub-molecular microscopic length scales or macroscopic length scales exceeding the droplet diameter [48]. Consequently, it raises the hypothesis that the standard hydrodynamic theory, which Eq. (23) is derived from, may not adequately characterize the internal flow at these conditions. Note that for the estimates, Stokes flow has been assumed, which is not applicable. The estimation of the contributions of wedge and bulk viscous force is also influenced by the shape of the droplet. Equations (23) and (24), however, assume a droplet shape which can be well approximated by a semi-sphere, with a circular contact area. Clearly, this approximation does not hold for fast-moving water droplets, particularly at higher substrate inclinations, as shown in Fig. 5. Nonetheless, the observed droplet distortion alone cannot account for the significant discrepancies, as the simulated droplets at low inclinations do not undergo substantial deformation, yet discrepancies persist. While viscous force is expected to be proportional to the droplet velocity, the simulation results exhibit a slight non-linearity in the viscous force over increasing droplet velocities. This can be attributed to the increase in the wetted area as the sliding velocity rises [17]. Another notable deviation is observed, where the bulk viscous force from simulation yields significantly higher values than expected. This discrepancy arises from Eq. 24, which assumes wall-normal gradient of the velocity field to be proportional to U/R, implying that the internal flow within the droplet away from the contact area resembles rigid rotation [49]. However, at higher velocities and for Bond numbers $\text{Bo} = \frac{\rho_L R^2 g}{\sigma} \approx 1$, the droplet deformation during acceleration leads to increased internal shear, which appears to be underestimated when using such a simplifying assumption.

The analysis is extended to water-glycerol droplets, revealing a greater contribution of wedge viscous force in comparison to water droplets. By employing Eq. (26), we compare the estimated wedge-to-bulk viscous force ratio with simulation results, demonstrating improved accuracy in Fig. 17.

We further investigate the velocity-dependent wedge and bulk viscous force, see Fig. 18. Notably, the estimation of wedge viscous force is considerably improved in comparison to water droplets. By fitting the results with Equation (23), the obtained value for L/L_s is approximately 1×10^6, which is physically plausible. This suggests that Stokes flow conditions are a suitable assumption for these droplets, given their slow motion and internal flow velocities. Regarding bulk viscous force, Eq. (24) still underestimates the results, albeit achieving closer agreement than in water droplets. This observation indicates that the internal motion of water-glycerol droplets can be more accurately approximated by rigid rotational motion, as their velocities fall within the range of centimeters per second, and there is minimal droplet deformation.
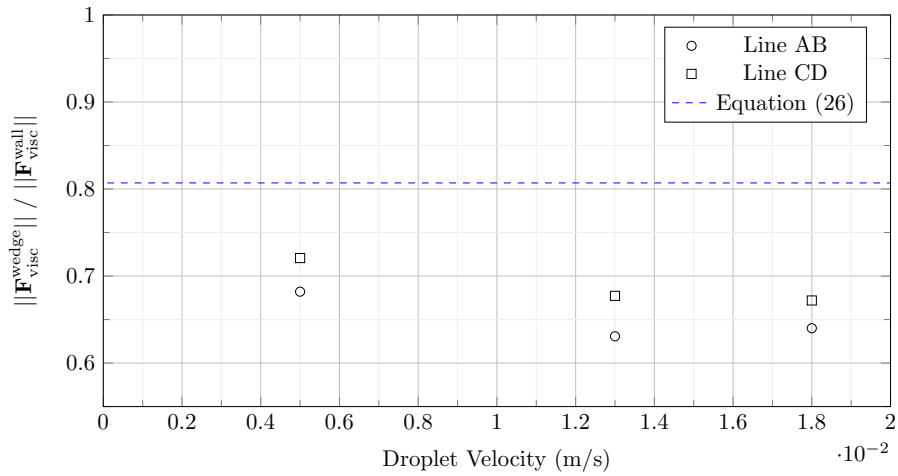
Fig. 17 Comparison of the relative contribution of the wedge to the total viscous force at various droplet velocities—Estimate according to Kim et al. [13] versus Results from local simulation data for a water-glycerol droplet (85 wt%)
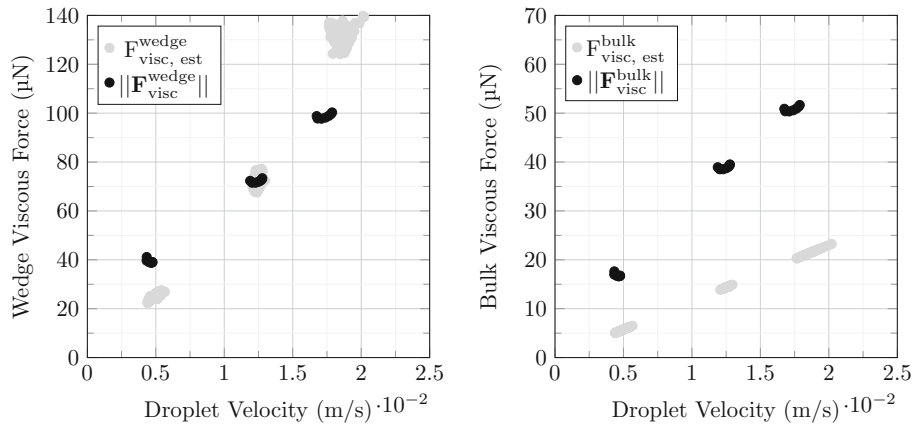

Fig. 18 Wedge (left) and bulk (right) viscous forces exerted by a water-glycerol droplet, for the investigated range of droplet velocities

5.3 Influence of internal flow on total viscous force

We explore the impact of time elapsed since the droplet release on the viscous force. We begin with a water droplet at a 30° inclination, allowing it to move until it reaches a velocity. Subsequently, we repeat this experiment with the same droplet, but this time at a steeper inclination of 50°. When it reaches the same velocity, we examine whether or not the viscous force remains the same. This comparison is presented in Fig. 19.

Throughout the droplet motion, we observe that the lower inclination case exhibits the largest viscous force, for the same droplet velocity. According to Eqs. (23) and (24), one would expect the viscous force to be identical for the same droplet physical properties and velocity, assuming nearly identical droplet shapes. To investigate this discrepancy in viscous force, we examine the viscous force density and internal flow for the 30° and 50° cases at a sliding velocity of 0.1 m/s, as shown in Fig. 20. The comparison reveals distinctly different internal flows for the two droplets due to the different observation times at which they reach the same velocity. These internal flow variations contribute to the slight differences in viscous force between the two droplets, which are not accounted for in Eqs. (23) and (24).
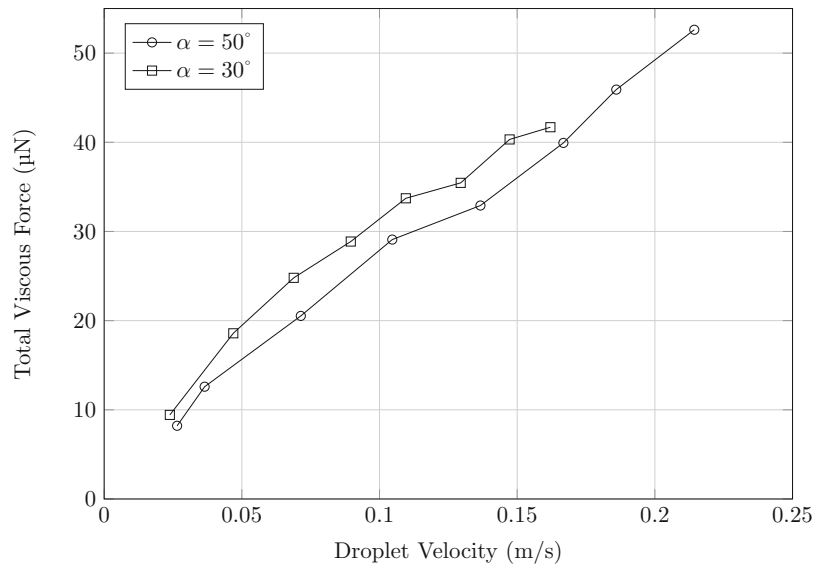
Fig. 19 Comparison of the magnitude of total viscous forces for a droplet on a substrate at different inclinations (30° and 50°)
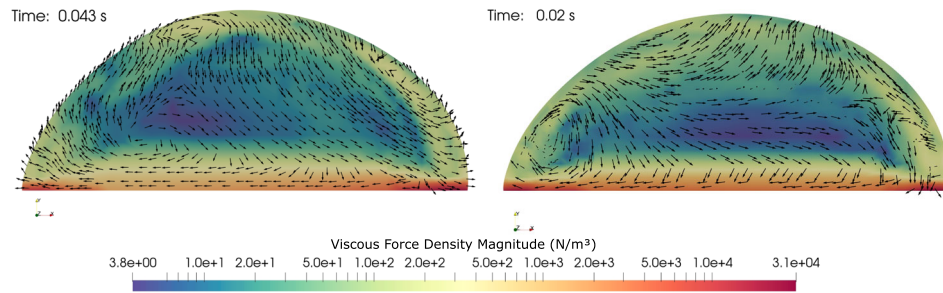
Fig. 20 Comparison between the internal flow pattern of water droplet when moving on a tilted substrate with 30° and 50° inclination and reaching the same velocity. The velocity vectors shown here are computed in a co-moving reference frame

6 Summary and conclusion

Three-dimensional simulations are conducted to investigate the contributions of wedge and bulk viscous forces acting on tilted planar substrates from droplets moving on them. The simulations involve water and water-glycerol droplets and plates at various inclinations.

Our study reveals a nonuniform distribution of local viscous forces within the droplet, with the largest viscous friction occurring near the contact line, at the droplet front and rear edges. Existing estimates of these forces require caution, as they underestimate wedge and bulk viscous force for droplets moving at high velocities, especially for water droplets. The presence of inertial effects in the bulk is not accounted for in these correlations, resulting in an underestimation of the bulk viscous force. Additionally, it is demonstrated that droplets moving at the same velocity may exhibit different viscous forces due to differences in their internal flow patterns.

Declarations

Conflict of interest The authors declare that they have no known competing financial interests or personal relationships that could have appeared to influence the work reported in this paper.

Authors' contributions F.B.: Conceptualization, Data curation, Formal analysis, Investigation, Methodology, Software, Validation, Visualization, Project administration, Writing - original draft, and Writing—review & editing. X. L.: Conceptualization, Formal analysis, Investigation, Methodology, Resources, and Writing—review & editing. M.Y.: Formal analysis, Investigation, Validation, and Visualization. R.B.: Conceptualization, Formal analysis, Funding acquisition, Project administration, Resources, Supervision, and Writing—review & editing. H.-J.B.: Conceptualization, Formal analysis, Funding acquisition, Project administration, Resources, Supervision, and Writing - review & editing. H.M.: Conceptualization, Formal analysis, Methodology, Software, Validation, Funding acquisition, Project administration, Resources, Supervision, and Writing—review & editing.

Data availability Source datasets for all figures in the main text are available from the corresponding authors upon request.

References

1. Hattori, T., Sakai, M., Akaike, S., et al.: Numerical simulation of droplet sliding on an inclined surface using moving particle semi-implicit method. Comput. Part. Mech. **5**(4), 477–491 (2018). https://doi.org/10.1007/s40571-018-0184-9
2. Klimanek, A.: Numerical modelling of natural draft wet-cooling towers. Arch. Comput. Methods Eng. **20**(1), 61–109 (2013). https://doi.org/10.1007/s40571-018-0184-9
3. Seemann, R., Brinkmann, M., Pfohl, T., et al.: Droplet based microfluidics. Rep. Prog. Phys. **75**(1), 016601 (2011). https://doi.org/10.1088/0034-4885/75/1/016601
4. Liu, C., Sun, Y., Huanng, J., et al.: External-field-induced directional droplet transport: a review. Adv. Colloid Interface Sci. **295**, 102502 (2021). https://doi.org/10.1016/j.cis.2021.102502
5. Yilbas, B.S., Hassan, G., Al-Qahtani, H., et al.: Stretchable hydrophobic surfaces and self-cleaning applications. Sci. Rep. **9**(1), 1–13 (2019). https://doi.org/10.1038/s41598-019-50982-8
6. Milionis, A., Krishnan, K.G., Loth, E., et al.: Dynamic wetting of human blood and plasma on various surfaces. Colloids Surf. B **166**, 218–223 (2018). https://doi.org/10.1016/j.colsurfb.2018.03.027
7. Mahrous, E., Roy, R.V., Jarauta, A., et al.: A two-dimensional numerical model for the sliding motion of liquid drops by the particle finite element method. Phys. Fluids **33**(3), 032117 (2021). https://doi.org/10.1063/5.0039517
8. Schnitzer, O., Davis, A.M.J., Yariv, E.: Rolling of non-wetting droplets down a gently inclined plane. J. Fluid Mech. (2020). https://doi.org/10.1017/jfm.2020.650
9. Yariv, E., Schnitzer, O.: Speed of rolling droplets. Phys. Rev. Fluids **4**(9), 093602 (2019). https://doi.org/10.1103/physrevfluids.4.093602
10. Ngan, C.G., Dussan V, E.B.: The moving contact line with a 180° advancing contact angle. Phys. Fluids **27**(12), 2785 (1984) https://doi.org/10.1063/1.864591
11. Tadmor, R., Bahadur, P., Leh, A., et al.: Measurement of lateral adhesion forces at the interface between a liquid drop and a substrate. Phys. Rev. Lett. **103**(26), 266101 (2009). https://doi.org/10.1103/physrevlett.103.266101
12. Li, X., Silge, S., Saal, A., et al.: Adaptation of a styrene-acrylic acid copolymer surface to water. Langmuir **37**(4), 1571–1577 (2021). https://doi.org/10.1021/acs.langmuir.0c03226
13. Kim, H.-Y., Lee, H.J., Kang, B.H.: Sliding of liquid drops down an inclined solid surface. J. Colloid Interface Sci. **247**(2), 372–380 (2002). https://doi.org/10.1006/jcis.2001.8156
14. Backholm, M., Molpeceres, D., Vuckovac, M., et al.: Water droplet friction and rolling dynamics on superhydrophobic surfaces. Commun. Mater. (2020). https://doi.org/10.1038/s43246-020-00065-3
15. Gao, N., Geyer, F., Pilat, D.W., et al.: How drops start sliding over solid surfaces. Nat. Phys. **14**(2), 191–196 (2017). https://doi.org/10.1038/nphys4305
16. Suda, H., Yamada, S.: Force measurements for the movement of a water drop on a surface with a surface tension gradient. Langmuir **19**(3), 529–531 (2002). https://doi.org/10.1021/la0264163
17. Timonen, J.V.I., Latikka, M., Ikkala, O., et al.: Free-decay and resonant methods for investigating the fundamental limit of superhydrophobicity. Nat. Commun. (2013). https://doi.org/10.1038/ncomms3398
18. Snoeijer, J.H., Andreotti, B.: Moving contact lines: scales, regimes, and dynamical transitions. Annu. Rev. Fluid Mech. **45**(1), 269–292 (2013). https://doi.org/10.1146/annurev-fluid-011212-140734
19. Hattori, T., Koshizuka, S.: Numerical simulation of droplet behavior on an inclined plate using the Moving Particle Semi-implicit method. Mech. Eng. J. **6**(5), 19–002041900204 (2019). https://doi.org/10.1299/mej.19-00204
20. Dupont, J.-B., Legendre, D.: Numerical simulation of static and sliding drop with contact angle hysteresis. J. Comput. Phys. **229**(7), 2453–2478 (2010). https://doi.org/10.1016/j.jcp.2009.07.034

21. Linder, N., Criscione, A., Roisman, I.V., Marschall, H., Tropea, C.: 3d computation of an incipient motion of a sessile drop on a rigid surface with contact angle hysteresis. Theor. Comput. Fluid Dyn. **29**(5–6), 373–390 (2015). https://doi.org/10.1007/s00162-015-0362-9

22. Maglio, M., Legendre, D.: Numerical simulation of sliding drops on an inclined solid surface. In: Computational and Experimental Fluid Mechanics with Applications to Physics, Engineering and the Environment, pp. 47–69. Springer, Berlin (2014). https://doi.org/10.1007/978-3-319-00191-3_3

23. Derksen, J.J., Komrakova, A.E.: Multiscale simulations of sliding droplets. Acta Mech. **230**(2), 657–666 (2018). https://doi.org/10.1007/s00707-018-2264-6

24. Yue, P., Zhou, C., Feng, J.J.: Sharp-interface limit of the Cahn–Hilliard model for moving contact lines. J. Fluid Mech. **645**, 279–294 (2010). https://doi.org/10.1017/s0022112009992679

25. Yue, P.: Thermodynamically consistent phase-field modelling of contact angle hysteresis. J. Fluid Mech. **899**, A15 (2020). https://doi.org/10.1017/jfm.2020.465

26. Jamshidi, F., Heimel, H., Hasert, M., et al.: On suitability of phase-field and algebraic volume-of-fluid OpenFOAM®solvers for gas-liquid microfluidic applications. Comput. Phys. Commun. **236**, 72–85 (2019). https://doi.org/10.1016/j.cpc.2018.10.015

27. Bodziony, F., Wörner, M., Marschall, H.: The stressful way of droplets along single-fiber strands: a computational analysis. Phys. Fluids **35**(1), 012110 (2023). https://doi.org/10.1063/5.0131032

28. Huang, Z., Lin, G., Ardekani, A.M.: A consistent and conservative phase-field method for multiphase incompressible flows. J. Comput. Appl. Math. **408**, 114116 (2022). https://doi.org/10.1016/j.cam.2022.114116

29. Abels, H., Garcke, H., Grün, G.: Thermodynamically consistent, frame indifferent diffuse interface models for incompressible two-phase flows with different densities. Math. Models Methods Appl. Sci. **22**(03), 1150013 (2012). https://doi.org/10.1142/s0218202511500138

30. Cahn, J.W., Hilliard, J.E.: Free energy of a nonuniform system. III. Nucleation in a two-component incompressible fluid. J. Chem. Phys. **31**(3), 688–699 (1959). https://doi.org/10.1063/1.1730447

31. Jacqmin, D.: Contact-line dynamics of a diffuse fluid interface. J. Fluid Mech. **402**, 57–88 (2000). https://doi.org/10.1017/s0022112099006874

32. Yue, P., Feng, J., Liu, C., et al.: A diffuse-interface method for simulating two-phase flows of complex fluids. J. Fluid Mech. **515**, 293–317 (2004). https://doi.org/10.1017/s0022112004000370

33. Fink, V., Cai, X., Stroh, A., et al.: Drop bouncing by micro-grooves. Int. J. Heat Fluid Flow **70**, 271–278 (2018). https://doi.org/10.1016/j.ijheatfluidflow.2018.02.014

34. Cai, X., Marschall, H., Wörner, M., et al.: Numerical simulation of wetting phenomena with a phase-field method using OpenFOAM®. Chem. Eng. Technol. **38**(11), 1985–1992 (2015). https://doi.org/10.1002/ceat.201500089

35. Wörner, M., Samkhaniani, N., Cai, X., et al.: Spreading and rebound dynamics of sub-millimetre urea-water-solution droplets impinging on substrates of varying wettability. Appl. Math. Model. **95**, 53–73 (2021). https://doi.org/10.1016/j.apm.2021.01.038

36. Samkhaniani, N., Stroh, A., Holzinger, M., et al.: Bouncing drop impingement on heated hydrophobic surfaces. Int. J. Heat Mass Transf. **180**, 121777 (2021). https://doi.org/10.1016/j.ijheatmasstransfer.2021.121777

37. Gilet, T., Terwagne, D., Vandewalle, N.: Droplets sliding on fibres. Eur. Phys. J. E **31**(3), 253–262 (2010). https://doi.org/10.1140/epje/i2010-10563-9

38. Biance, A.-L., Clanet, C., Quéré, D.: First steps in the spreading of a liquid droplet. Phys. Rev. E **69**, 1 (2004). https://doi.org/10.1103/physreve.69.016301

39. Bagheri, M., Stumpf, B., Roisman, I.V., et al.: Interfacial relaxation-Crucial for phase-field methods to capture low to high energy drop-film impacts. Int. J. Heat Fluid Flow **94**, 108943 (2022). https://doi.org/10.1016/j.ijheatfluidflow.2022.108943

40. Tadmor, R.: Line energy and the relation between advancing, receding, and young contact angles. Langmuir **20**(18), 7659–7664 (2004). https://doi.org/10.1021/la049410h

41. Li, X., Bodziony, F., Yin, M., Berger, R., Butt, H.-J., Marschall, H.: Kinetic drop friction. Nat. Commun. **14**(1), 4571 (2023). https://doi.org/10.1038/s41467-023-40289-8

42. Dussan, E., Davis, S.: On the motion of a fluid-fluid interface along a solid surface. J. Fluid Mech. **65**(1), 71–95 (1974). https://doi.org/10.1017/s0022112074001261

43. Gennes, P.G.: Wetting: statics and dynamics. Rev. Mod. Phys. **57**(3), 827–863 (1985). https://doi.org/10.1103/revmodphys.57.827

44. Moffatt, H.K.: Viscous and resistive eddies near a sharp corner. J. Fluid Mech. **18**(1), 1–18 (1964). https://doi.org/10.1017/s0022112064000015

45. Carlson, A., Do-Quang, M., Amberg, G.: Dissipation in rapid dynamic wetting. J. Fluid Mech. **682**, 213–240 (2011). https://doi.org/10.1017/jfm.2011.211

46. Li, X., Bista, P., Stetten, A.Z., et al.: Spontaneous charging affects the motion of sliding drops. Nat. Phys. **18**(6), 713–719 (2022). https://doi.org/10.1038/s41567-022-01563-6

47. Dussan, E.B.: On the spreading of liquids on solid surfaces: static and dynamic contact lines. Annu. Rev. Fluid Mech. **11**(1), 371–400 (1979). https://doi.org/10.1146/annurev.fl.11.010179.002103

48. Blake, T.D.: The physics of moving wetting lines. J. Colloid Interface Sci. **299**(1), 1–13 (2006). https://doi.org/10.1016/j.jcis.2006.03.051

49. Mahadevan, L., Pomeau, Y.: Rolling droplets. Phys. Fluids **11**(9), 2449–2453 (1999). https://doi.org/10.1063/1.870107